2012

Coaxial cable Bragg grating

Jie Huang
Missouri University of Science and Technology, jieh@mst.edu

Department:

COAXIAL CABLE BRAGG GRATING

by

JIE HUANG

A THESIS

Presented to the Faculty of the Graduate School of the

MISSOURI UNIVERSITY OF SCIENCE AND TECHNOLOGY

In Partial Fulfillment of the Requirements for the Degree

MASTER OF SCIENCE IN ELECTRICAL ENGINEERING

2012

Approved by

Dr. Hai Xiao, Advisor
Dr. Jun Fan
Dr. Hai-Lung Tsai

ABSTRACT

In order to ensure the continued safe and reliable operation of various civil structures, such as dams, bridges, and buildings, in situ strain monitoring is of great importance, especially for structures that may experience large strains. A new coaxial cable Bragg grating (CCBG) is developed as a strain sensor and the sensor's capacity for large range strain measurement is demonstrated for the first time. The sensor device is comprised of regularly spaced periodic discontinuities along a coaxial cable. The discontinuities are fabricated using a computer numerical controlled (CNC) machine to drill holes in the cable. Each discontinuity generates a weak reflection to the electromagnetic wave propagating inside the cable. Superposition of these weak reflections produces a strong reflection at discrete frequencies that can be explained by Bragg grating theory. A positive feedback oscillation system is also developed to enhance the measurement accuracy. The Q-factor was enhanced by 3500 times in this case. By monitoring the resonant frequency shift of the sensor's reflection or transmission spectra using the oscillation system, strain measurement sensitivity of 20με and a dynamic range of 50000με (5%) were demonstrated for axial strain measurements. The temperature responses of various types of CCBGs have also been investigated. The experimental results show that the CCBG sensors perform well for large strain measurement needed in structural health monitoring (SHM).

ACKNOWLEDGMENTS

I would like to take this opportunity to thank all those people who helped me with the successful completion of my research. First, I would like to express my gratitude to my advisor Dr. Hai Xiao, without whom this research could be considered incomplete. I thank him for giving me a chance to work with the group and for his continued support with valuable advice and encouragement. His subtle guidance and patience have made a great impact on this research and me.

I would like to thank Dr. Jun Fan who is the leader of this project and provided me lots of precious guidance.

I am grateful to Dr. Jun Fan, Department of Electrical and Computer Engineering and Dr. Hai-Lung Tsai, Department of Mechanical and Aerospace Engineering for being my committee members.

I also would like to take this opportunity to thank my colleagues in my group for being supportive all the time.

I would also like to thank my parents and my wife Lingyu Chi for everything they have done for me. Finally, I would like to thank the sponsor for this project: U.S. National Science Foundation.

TABLE OF CONTENTS

LIST OF ILLUSTRATIONS

Page

LIST OF ABBREVIATIONS

Abbreviation	Full name
SHM	Structural health monitoring
FOS	Fiber optic sensors
EFPI	Extrinsic Fabry-Perot interferometer
FBG	Fiber Bragg grating
CCBG	Coaxial cable Bragg grating
EM	Electromagnetic
MZI	Mach-Zehnder interferometer
PC	Photonic crystal
RF	Radio frequency
TDR	Time-domain reflectometry
T-matrix	Transfer matrix
Q-factor	Quality factor
CNC	Computer numerical controlled
VNA	Vector network analyzer
SNR	Signal-to-noise ratio
DC	Directional coupler
EDF	Erbium-doped fiber
RBW	Resolution bandwidth
IFBW	Intermediate frequency bandwidth
CTE	Coefficient of thermo-expansion

1. INTRODUCTION

1.1. BACKGROUND AND REVIEW

Each year in U.S., federal, state, and local governments spend billions of dollars to maintain, upgrade, repair and renovate various civil structures such as buildings, bridges, dams, tunnels, pipelines and offshore platforms. The factors that affect the integrity of these large and complex civil infrastructures cannot be perfectly predicted. As a result, the degradation process of the structures must be monitored in some form. Embedded sensors have the most desired capability for structural health monitoring (SHM) [1, 2]. These sensors are used for measurement of various structural and environmental parameters such as strain, force, crack, deflection, vibration and corrosion under normal and extreme conditions for in situ assessment of the health of the structures.

1.1.1. The Need for Large Strain Sensors in SHM. Reinforced concrete and steel structures have been widely used in civil infrastructure [3]. Their ductile behavior and extensive deformability provide the designed functionality under normal loads and ensure the structural safety under extreme loads associated with natural and man-made disasters. Under normal loads, these structures are subjected to strains of less than 2,000 με and often behave elastically. Under extreme loads such as earthquakes and landslides, they behave elastically, experiencing excessive deformations or strains in the order of 1% to 10%. Ideal embeddable strain sensors need to have high resolution for monitoring and understanding the structural behaviors under normal loads, while they must be robust to survive and have a large dynamic range to operate under extreme conditions.

The last three decades have witnessed many breakthrough sensor technologies (e.g., fiber optic sensors (FOS) and MEMS sensors) [4-10]. However, SHM still faces a number of challenges imposed by the inadequacy of sensors. In particular, currently available embeddable sensors have insufficient dynamic range while maintaining the required high resolution for accurate measurement of large strains and forces. As such, the structural limit states such as concrete cracking and steel yielding processes are still not sufficiently monitored and the progressive collapse of structural systems under extreme loads is still not well understood. Existing sensors also lack the necessary robustness to survive the harsh conditions during sensor installation/embedment,

structure construction and operation under extreme conditions, leaving a major capability gap in SHM. As such, post seismic and disaster SHM is still under-addressed due to the lack of robust sensors with large dynamic range. Innovative research is required to find a novel solution to fill the capability gaps.

1.1.2. Review of Current Strain Sensors used in SHM. The development of large strain sensors has recently attracted worldwide attentions. To this endeavor, the main challenge remains in achieving a large dynamic range while maintaining high resolution. Conventional strain sensors represented by electro-resistive strain gauges have the satisfactory resolution but a limited dynamic range of less than 1.5%. For strains higher than 2%, extensometers, linear variable differential transformers [11], and grating based mark tracking technique are commonly used [12-14]. They can typically measure a strain of up to 5% with low resolution of 0.45%. A common issue associated with these large strain sensors resides in the difficulty for sensor embedment into the structure due to the large size of the transducer. Other issues include electrical wiring/connection, poor stability and large temperature cross-sensitivity.

In the past two decades, fiber optic sensors have found many successful applications in SHM due to their unique advantages such as compactness, high resolution, and immunity to electromagnetic interference, remote operation and multiplexing capability [8]. In general, fiber sensors have relatively small dynamic range due to the limited deformability of silica glass. Various strain transfer mechanisms have been investigated to extend the dynamic range of the sensor devices. For example through a specially-designed sensor package, a high strain resolution of 10 με within a large dynamic range (12,000 με) has been demonstrated using an extrinsic Fabry-Perot interferometer (EFPI) [15]. However, when embedded into the structure, the signal transmission line (i.e., the optical fiber) can easily break when it is subjected to a large strain (about 1%) and/or a shear force, causing serious challenges for sensor installation and operation. As such, fiber optic sensors have restricted applications in heavy duty or large strain measurement.

1.2. THE SEARCH FOR A MORE ROBUST CABLE

1.2.1. Plastic Optical Fibers. In the effort of searching for more robust transmission cables, plastic optical fibers have been explored for sensor development by taking the advantage of their inelastic nature. Plastic fiber sensors with a strain measurement range of up to 15.8% have been reported [16-19]. However, current plastic fibers have poor optical transmission and waveguiding properties, making it difficult to fabricate high performance sensors. The strong thermo-optic coupling effect and a large thermal expansion coefficient have also resulted in a large temperature-strain cross sensitivity of the sensors.

1.2.2. Coaxial Cables. Another candidate is coaxial cable. As shown in Fig. 1.1, a coaxial cable consists of an inner and an outer conductor sandwiched by a tubular insulating layer typically made of a flexible material with a high dielectric constant [20]. The coaxial cable and optical fiber are the two basic forms of waveguiding structures that have been widely used in telecommunications for transmitting signals over a long distance [21, 22]. These two types of cables share the common fundamental physics governed by the same electromagnetic (EM) theory, except that the frequencies of the EM waves supported by them are quite different. In comparison with optical fibers, coaxial cables can survive a large longitudinal strain and are relatively resistant to lateral force and bending.

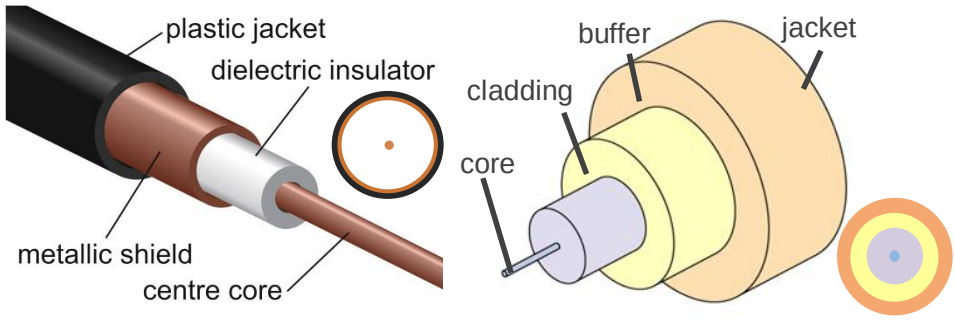

Figure 1.1. Fiber versus coaxial cable.

An interesting question is whether some of the successful concepts of fiber sensors can be adopted onto the coaxial cable. For example, can a Bragg resonance device be implemented using a coaxial cable so that it functions in the similar way as an FBG sensor? This is not only interesting from the device physics perspective but also motivated by the application potentials that the new coaxial cable Bragg device might provide a solution for some challenging issues (e.g., the fragility) faced by fiber optic sensors.

1.3. A NOVEL CONCEPT OF CCBG

1.3.1. Review of Relevant Technologies of Coaxial Cable. Pioneering research has already started to explore various coaxial cable devices mimicking their optical fiber counterparts. Inspired by the well-known optical fiber Mach-Zehnder interferometer (MZI), the coaxial cable based MZI implementations have been demonstrated and the superluminal and negative group velocities in the radio frequency (RF) regime were observed experimentally [23]. RF bandgap structures have also been explored to mimic the photonic crystal (PC) device that has found many interesting applications such as wavelength specific filters, reflectors, waveguides, light trappers, and superlenses. In one case, alternating 50 Ω and 75 Ω coaxial cable segments were connected in a row to create periodic impedance variations along the cable length to form the so called coaxial PC [24]. Experimental evidence such as bandgaps, sub- or super-luminal velocities and defect modes were observed and investigated in the RF regime [25, 26].

Recently, a coaxial cable sensor was demonstrated and investigated for health monitoring of concrete structures. The sensor was fabricated with tightly wrapped tin-plated steel spiral covered with solder. The cracks that developed within concrete structures could cause out of contact of the steel spirals. This topology change will result in an impedance discontinuity that can be measured using time-domain reflectometry (TDR) [27, 28]. The reported sensor has low resolution and works only for detection of extreme large load (e.g., cracks) in the concrete. In addition, the method is prone to noise and random reflections generated during cable deployment and it does not have a

deterministic relation between the signal and the applied load. Nevertheless, the work successfully proved the feasibility of using coaxial cable sensor for SHM.

1.3.2. The CCBG Concept. A novel coaxial cable sensor for SHM based on the concept of coaxial cable Bragg grating (CCBG) is proposed in this project. It is inspired by the well-known FBG - a very successful device with tremendous applications in SHM [29, 30]. An FBG consists of weak periodic reflective index perturbations in the core along the fiber. Each index perturbation produces a weak reflection and the constructive interference among these periodic reflections generates strong reflections at discrete wavelengths. FBG arrays can be embedded into materials and structures to allow distributed measurement of various parameters such as load, strain, temperature, and vibration, from which the health condition of the structure can be assessed and tracked on a real-time basis [31-34]. Unfortunately FBG sensors have limited dynamic range and cannot be used for structure monitoring under extreme loads as discussed earlier.

Figure 1.2 shows the concept and operation principle of a CCBG device. As illustrated in Fig. 1.2 (a), the proposed CCBG sensor is realized by introducing periodic impedance discontinuities in a coaxial cable. Similar to an FBG, each discontinuity generates a weak reflection to the EM wave propagating inside the cable. Assuming all the discontinuities are the same, the overall reflection can be obtained based on the well-established transmission line theory [35],

$$reflection\ \ spectrum = \frac{\Gamma e^{-j2\beta\Lambda}\left\{1-\left[(1+\Gamma)^2 e^{-j2\beta\Lambda}\right]^N\right\}}{1-(1+\Gamma)^2 e^{-j2\beta\Lambda}} \tag{1}$$

where N is the number of discontinuities in the cable; β is the propagation constant of the EM wave travelling inside the cable; Λ is the period of the grating; and, Γ is the reflection coefficient of each individual discontinuity. Equation (1) indicates that the accumulation of the individual reflections eventually results in strong reflections at discrete frequencies where the superposition is in-phase (i.e., $\beta\Lambda$ is the integer multiples of π). A typical reflection spectrum is illustrated in Fig. 1.2(b) based on the conceptual approximation of Equation (1). An equation can also be derived for the overall

transmission spectrum, which has resonant valleys corresponding to the resonant peaks in the reflection spectrum as illustrated in Fig. 1.2(c). The resonant frequencies of the reflection and transmission spectra of the CCBG are a function of the period of the grating. Applying strain on the CCBG will change the grating period and thus shift the resonant frequencies. The device can be interrogated by sending an EM wave from one end of the cable and analyze either the reflection (from the input port through a splitter or circulator) or the transmission spectrum (from the opposite end of the input port).

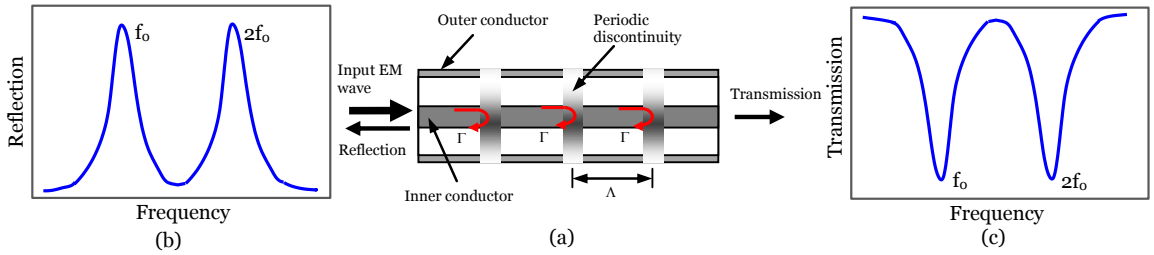

Figure 1.2. Concept and operation principle of a CCBG device. (a) Schematic illustration of the CCBG device, (b) illustration of the reflection spectrum, (c) illustration of the transmission spectrum.

1.4. RESEARCH OBJECTIVE

From the discussion above, the main objective of this thesis is to design and fabricate CCBG sensor for measurement of large strains. To be detailed, the specific objectives are to:

1) Investigate the fundamental physics and theoretical model of the device.
2) Investigate the optimal techniques and processes to generate the periodic discontinuities and fabricate high quality CCBG devices.
3) Develop an effective, noise-insensitive signal processing method.
4) Demonstrate the device for large strain measurement and characterize the temperature-strain crosstalk.

1.5. THESIS OVERVIEW

This thesis focuses on the design, fabrication and characterization of a newly developed CCBG sensor in the application of SHM. The contents of the thesis are arranged as follows:

Section 2 focuses on the fundamental physics and theoretic model of the proposed CCBG device. A transfer matrix (T-matrix) method is developed to numerically simulate the performance of CCBG.

Section 3 focuses on the fabrication method of the proposed CCBG device. A hole-drilling method is developed to fabricate periodic discontinuities along the coaxial cable. To further enhance the quality factor (Q-factor), a coiled CCBG is also developed.

Section 4 focuses on the sensing mechanism and experimental results (strain and temperature) of the CCBGs. Experimental results match well with the theoretic predictions.

The conclusions and future work are summarized in Section 5.

2. FUNDAMENTAL PHYSICS AND THEORETIC MODEL

2.1. FUNDAMENTAL PHYSICS OF CCBG

As shown in Fig. 2.1, the proposed CCBG is made by inducing air-holes at periodic distance along the coaxial cable. The air-hole perturbs the electromagnetic (EM) waves propagating in the otherwise continuous coaxial transmission line, resulting in a localized characteristic impedance change (air/dielectric discontinuity point) and thus a partial reflection from the impedance discontinuity. Assuming that all the discontinuities are identical, each hole generates a partial reflection with a reflection coefficient Γ along the cable as shown in Fig. 2.1. Further assuming that the initial phase at the first hole is zero and the cable is lossless, as the voltage wave travels along the coaxial cable, the accumulated reflection (S_{11}) can be derived by the following equation [36],

$$S_{11} = \frac{1}{V_0} \sum_{n=0}^{N-1} V_r[n] e^{-j2\beta n\Lambda} \tag{2}$$

where V_0 is the input voltage wave, N is the total number of holes on the cable, $V_r[n]$ is the reflected voltage wave at the nth hole, β is the propagation constant of the EM wave travelling inside the coaxial cable, Λ is the period of grating, and 2βnΛ is the phase difference of a wave traveling a round-trip between the first and the n*th* hole. β can be calculated by $\beta = 2\pi f(LC)^{-1}$ or $\beta = 2\pi fn/c$, where f is the frequency of the EM wave, L and C are the distributed (per unit length) inductance and capacitance of the cable, respectively, n is the refractive index of the inner dielectric material and c is the speed of light in vacuum.

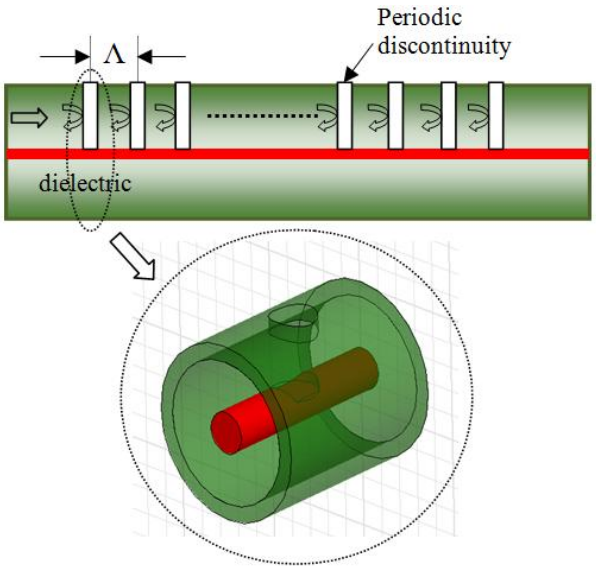

Figure 2.1. Concept and operation principle of a proposed CCBG device.

Assuming a small reflection coefficient of each hole, waves that are reflected more than once carry very little energy so that multiple reflections can be neglected. As a result, the reflection at the n_{th} hole, $V_r[n]$, can be calculated as

$$V_r[n] = V_0 \Gamma (1+\Gamma)^{2n} \tag{3}$$

where $(1+\Gamma)$ is the transmission coefficient of the hole. Therefore, the accumulated reflection given in Equation (2) can be simplified as

$$S_{11} = \frac{\Gamma[1-(1+\Gamma)^{2N-2} e^{-2\beta(N-2)\Lambda}]}{1-(1+\Gamma)^{2N} e^{-2\beta N\Lambda}} \tag{4}$$

Eq. (4) is similar to the well established transmission line theory in Eq. (1), indicates that the accumulation of the individual reflections eventually results in strong reflections at discrete frequencies where the superposition is in-phase.

2.2. TRANSFER MATRIX APPROXIMATION

We propose a two port transfer-matrix method (T-matrix) for numerically simulating the reflection and transmission spectra of the proposed CCBG. Figure 2.2 shows a segmentation approach for T-matrix method approximation. The entire cable is divided into multiple discontinuity segments and transmission-line segments, where a_n and b_n (n = 1, 2, 3…) are the voltage inputs and outputs parameters in each segment, respectively. Each discontinuity segment is investigated using a full-wave numerical solver (Ansoft HFSS) to compute its network parameters, for example the S-parameters. The 2×2 S-matrix of the discontinuity segment and transmission line segment can be written as

$$\begin{bmatrix} b_1 \\ b_2 \end{bmatrix} = [S_{DS}] \begin{bmatrix} a_1 \\ a_2 \end{bmatrix} = \begin{bmatrix} \Gamma & T \\ T & \Gamma \end{bmatrix} \begin{bmatrix} a_1 \\ a_2 \end{bmatrix}$$
$$\begin{bmatrix} b_3 \\ b_4 \end{bmatrix} = [S_{TS}] \begin{bmatrix} a_3 \\ a_4 \end{bmatrix} = \begin{bmatrix} 0 & e^{(\alpha + j\beta)\Lambda} \\ e^{(\alpha + j\beta)\Lambda} & 0 \end{bmatrix} \begin{bmatrix} a_3 \\ a_4 \end{bmatrix} \quad (5)$$

where $[S_{DS}]$ is the S-matrix of the discontinuity segment, Γ and T are the reflection and transmission coefficients of each dielectric/air discontinuity, respectively, $[S_{TS}]$ is the S-matrix of the transmission line segment, Λ is the length of each transmission line segment equaling to the period of the grating, α is the transmission loss of the cable, β is the propagation constant, Γ and T can be numerically simulated by a commercial full-wave solver including magnitude and phase. To make the matrix transfer in a two-port system, the S-matrix must be converted to a T-matrix, which can be mathematically calculated as

$$\begin{bmatrix} b_1 \\ a_1 \end{bmatrix} = [T_{DS}] \begin{bmatrix} a_2 \\ b_2 \end{bmatrix} = \begin{bmatrix} \frac{T^2 - \Gamma^2}{T^2} & \frac{\Gamma}{T} \\ -\frac{\Gamma}{T} & \frac{1}{T} \end{bmatrix} \begin{bmatrix} a_2 \\ b_2 \end{bmatrix}$$
$$\begin{bmatrix} b_3 \\ a_3 \end{bmatrix} = [T_{TS}] \begin{bmatrix} a_4 \\ b_4 \end{bmatrix} = \begin{bmatrix} e^{(\alpha + j\beta)\Lambda} & 0 \\ 0 & e^{(\alpha - j\beta)\Lambda} \end{bmatrix} \begin{bmatrix} a_4 \\ b_4 \end{bmatrix} \quad (6)$$

where $[T_{DS}]$ and $[T_{TS}]$ are the T-matrix of the discontinuity segment and transmission line segment, respectively. From (3), $[a_2, b_2]$ is the input of $[T_{DS}]$ but is also the output of $[T_{TS}]$ ($[b_3, a_3]$). As shown in Fig. 2.2, the right part of the discontinuity segment a_2 and b_2 are equivalent to the left part of the transmission line segment b_3 and a_3, respectively. As a result, the T-matrix has the transferring capability along the CCBG to model the device, and the final T-matrix can be written as

$$\begin{bmatrix} b_1 \\ a_1 \end{bmatrix} = \left([T_{DS}][T_{TS}] \right)^N \begin{bmatrix} a_N \\ b_N \end{bmatrix} = \left(\begin{bmatrix} \frac{T^2 - \Gamma^2}{T^2} e^{(\alpha + j\beta)\Lambda} & \frac{\Gamma}{T} e^{(\alpha - j\beta)\Lambda} \\ -\frac{\Gamma}{T} e^{(\alpha + j\beta)\Lambda} & \frac{1}{T} e^{(\alpha - j\beta)\Lambda} \end{bmatrix} \right)^N \begin{bmatrix} a_N \\ b_N \end{bmatrix} \tag{7}$$

where N is number of segments, or the number of discontinuities of the CCBG. After calculation of the final T-matrix of the CCBG, the last step is to convert the final T-matrix to S-matrix to find the input/output relation.

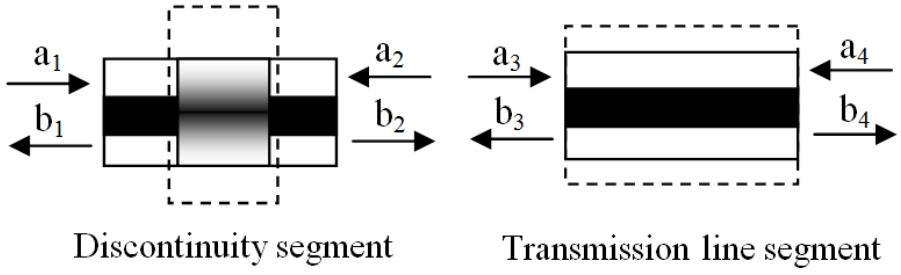

Figure 2.2. Segmentation approach for transfer matrix approximation.

Figure 2.3 plots the reflection and transmission coefficients (Γ and T) calculated by the full-wave simulation software. The inset in Fig. 2.1 shows the simulated air-hole model plotted by HFSS (what is this?). The diameter of the cylindrical air-hole was 2 mm and the depth was 2.1 mm, where the diameter of the cable's inner and outer conductors were 0.48 mm and 5 mm, respectively. A finite element method was used in the software to calculate the magnitude and phase of Γ and T as plotted in Fig. 2.3. The reflection coefficient (Γ) increased or the transmission coefficient (T) decreased as the interrogated frequency increased.

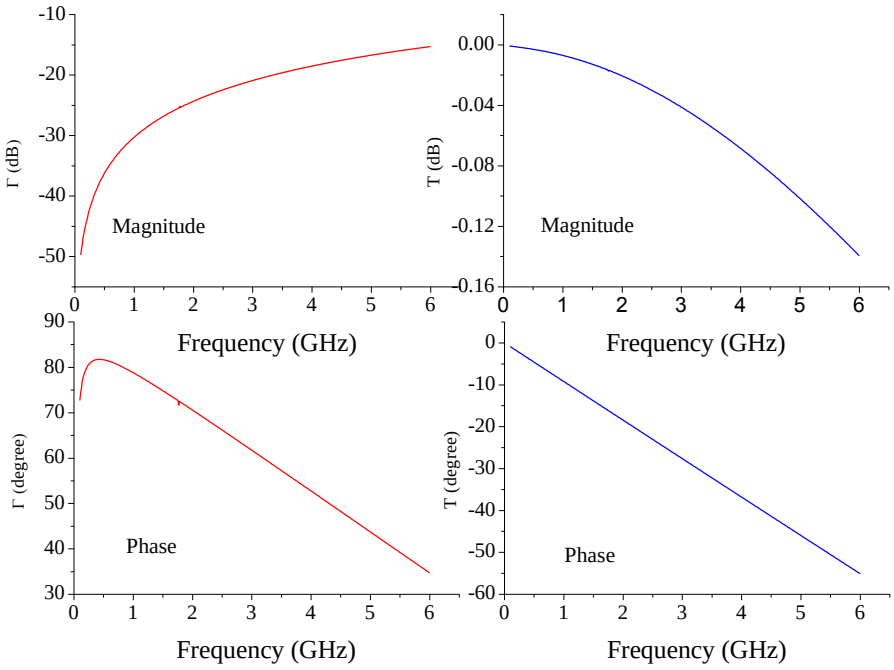

Figure 2.3. Calculated Γ and T of the discontinuity segment.

In the numerical simulation process, the dielectric of polyethylene n was set to be 1.5, and α was 0.04. Figure 2.4 plots the calculated reflection and transmission spectra of CCBG with different grating period (Λ) and number of discontinuities (N). Within the observation bandwidth of 0.1 GHz to 6 GHz, discrete resonances can be found at the

fundamental frequency of 1.339 GHz and its harmonics in both reflection and transmission spectra (top two figures in Fig. 2.4). In the transmission and reflection spectra, the strength of the resonant peaks or dips increased as the frequency increased. This can be qualitatively explained by the increasing reflection coefficient (Γ) as a function of frequency numerically simulated by Ansoft HFSS. We also found the quality-factor (Q-factor) of the resonant peaks or dips increased as N increased, which matched well with the FBG theory. The resonance bands of CCBGs with same grating period happened at the same location but the longer grating (large N) had stronger resonances with a higher Q-factor.

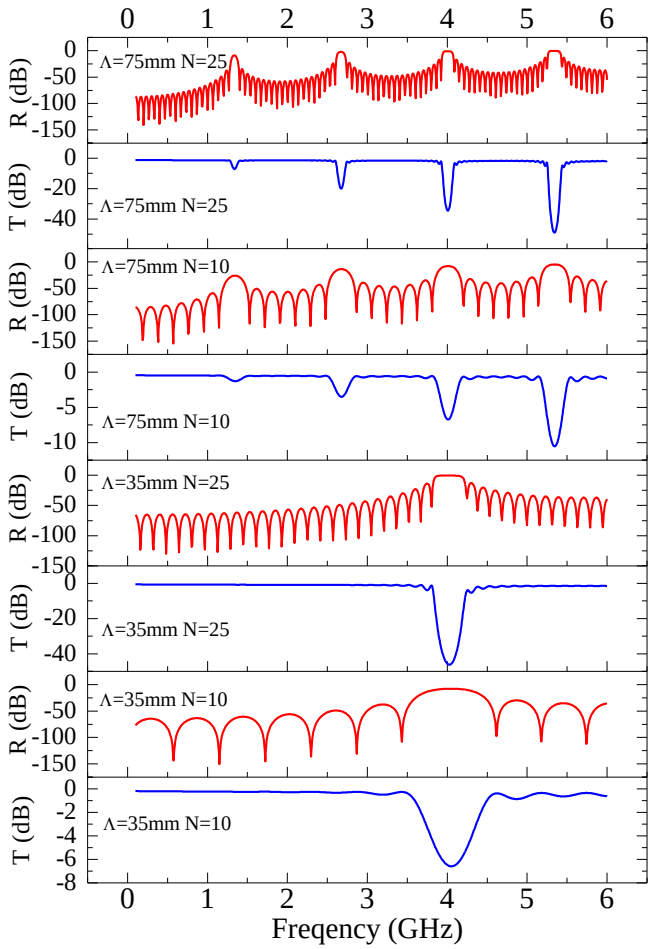

Figure 2.4. Calculated reflection and transmission spectra of CCBG by T-matrix method with different grating period (Λ) and number of discontinuities (N).

The resonance phenomenon can also be understood by the Bragg grating theory, similar to the well-studied case of FBG, where the forward propagating mode is coupled to the backward propagating mode in the waveguide at discrete frequencies satisfying the following Bragg condition [5],

$$\beta^{+} - \beta^{-} = 2\beta = \frac{2m\pi}{\Lambda} \quad \text{Or} \quad f_{res}^{m} = \frac{mc}{2n\Lambda} = \frac{m}{2\Lambda\sqrt{LC}} \tag{8}$$

where β^{+} and β^{-} are the propagation constant of the forward and backward traveling waves, respectively. They have the same magnitude but opposite signs. L and C represent the inductance and capacitance per unit length of the cable, respectively. The resonant frequency is denoted as f_{res}, and m is an integer representing the diffraction order of the grating. Using Eq. 8 to quickly calculate the parameters in Fig. 2.4, the resonant frequencies in the simulated spectra matched well with the calculation results.

2.3. SENSING MECHANISM OF CCBG

The applied axial strain in CCBG will induce changes in length (ΔL), inner dielectric radius (Δa) and square root of relative permittivity of the dielectric material ($\Delta\varepsilon_r^{1/2}$), which can be express as [37],

$$\begin{aligned} \Delta L &= L_s \varepsilon \\ \Delta a &= -va\varepsilon \\ \Delta\sqrt{\varepsilon_r} &= -\frac{\varepsilon_r^{3/2}}{2}\left[p_{12} - v(p_{11} + p_{12})\right]\varepsilon = -\sqrt{\varepsilon_r} P_{eff}\,\varepsilon \end{aligned} \tag{9}$$

where L_s is the sensing length of CCBG, ε is the applied strain, a is the inner dielectric radius, v is the Poisson ratio of the dielectric, $\varepsilon_r^{1/2}$ is the square root of relative permittivity of the dielectric, p_{11} and p_{12} are the Pockel's coefficients indicates that the relative permittivity of the inner dielectric will be changed (decreased) as stretching the cable, P_{eff} is the effective coefficient. Considering the EM wave propagating in the inner insulating material, the changes of dielectrics induced by the axial stress are the only

parameters taken into account. Comparing (8) and (9), the changes in L and $\varepsilon_r^{1/2}$ are the dominant elements inducing the change in spectra. The change in radius is not taken into account because there only exist single TEM mode supported by the coaxial cable as the frequency of several GHz range.

When a force is applied to the CCBG, a resonant frequency shift will be introduced because of the change of the cable dimension and dielectric constant of the inner dielectric material. The strain induced resonant frequency shift can be expressed as follow,

$$\Delta f = -\frac{L_s}{L_t}\left[\frac{\Delta L}{L_s} - \frac{\Delta\sqrt{\varepsilon_r}}{\sqrt{\varepsilon_r}}\right] f_{res}^m = -\frac{L_s}{L_t}\left(1 - P_{eff}\right)\varepsilon\, f_{res}^m \tag{10}$$

where Δf is the frequency shift of the interrogated resonant frequency induced by the axial strain, L_t is the total length of the cable under test. It is obvious that the resonant frequency decreases linearly to the applied strain. The reference values of p_{11}, p_{12} and ν of the polyethylene are 0.337, 0.327 and 0.27, respectively. After a quick calculation, P_{eff} was 0.2216 in this case. The stretch of the cable will increase the length of the cable but decrease the refractive index of the dielectric. Typically, the length under test will be equal to the length of CCBG, indicating that the strain-frequency slope can be simply written as,

$$\frac{\Delta f}{\mu\varepsilon} = -0.7784\times10^{-6}\, f_{res}^m\,(Hz/\mu\varepsilon) \tag{11}$$

where the unit of the slope is Hz/με. Assuming the interrogated resonant frequency is around 3 GHz, the resulted strain-frequency slope will be -2.335 KHz/με, which matched well with our preliminary result of -3 KHz/με in [14].

3. DEVELOPMENT OF CCBG MANUFACTURING TECHNIQUES

3.1. HOLE-DRILLING METHOD

The above investigations into the device physics reveal that the resonance behavior mainly results from the superposition of periodic reflections along the cable axis. The reflections are generated by impedance or refractive index discontinuities as a result of interruption in material properties such as the permittivity and permeability or in cable parameters such as the resistance, capacitance or inductance. As such, there are many potential methods to create the impedance discontinuities in a coaxial cable. Here we present a hole-drilling method to create periodic discontinuities along the cable axis.

Hole-drilling on a coaxial cable may degrade the mechanical strength of the cable. On the other hand, the hole-based CCBG sensor might open the opportunity for filling the holes with other types of materials for the purpose of temperature compensation. In addition, the device might be useful for measurement of other parameters such as corrosion and chemical concentration by refilling the holes with various functional materials. Therefore, it deserves a detailed investigation.

Figure 3.1 shows the proposed CCBG fabrication system. In order to precisely control the drilling shape, depth, grating period, a computer numerical controlled (CNC) drilling machine (Sherline P/N 8020A Model 2000) was used, where the minimum feeding step of the 3 axes is 100 μm. A vector network analyzer (VNA HP 8753ES) was used to in situ monitor the reflection spectrum during fabrication process. One end of the coaxial cable (50 Ω, Jamco Electronics, RG-58) was launched to the VNA and the other end was terminated with a 50 Ω resistor. A 1/12 inch drilling bit was chosen in this case. All the machines including VNA were controlled by a computer. The grating period was 25 mm and the number of discontinuities was 41 (in order to make the length of CCBG equaling to 1 m for the convenience of testing). The reflection spectra were recorded after each drilling point. The drilling depth was 2.1 mm and the out diameter of the cable was 5 mm. The coaxial cable was properly calibrated by VNA before fabrication and measurement.

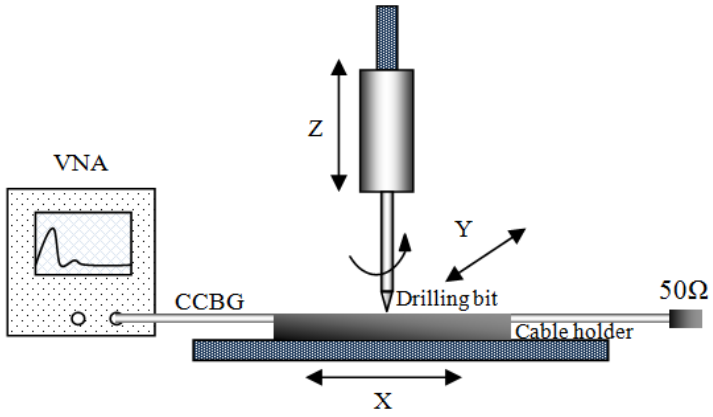

Figure 3.1. Proposed CCBG fabrication system.

Figure 3.2 plots the measured reflection spectra as the number of discontinuities (N) increased. The strength of the resonant peak increased as N increased. The spectrum of nonresonant frequencies stayed at the noise level, indicating that increasing the number of holes did not incur observable backward waves other than resonant frequency. The total number of discontinuities was 41 and the signal-noise-ratio (SNR) of the resonant peak in reflection spectrum was >14 dB in magnitude.

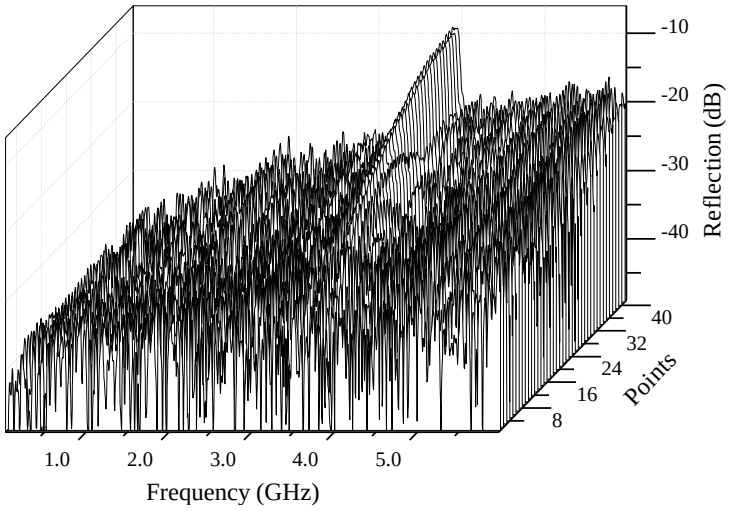

Figure 3.2. Measured reflection spectra as the number of discontinuities increased.

Figure 3.3 plots the reflection and transmission spectra of a fabricated CCBG. Within the frequency range of 100 KHz to 6 GHz, only one resonant frequency of 3.92 GHz (fundamental frequency) can be found in both reflection and transmission spectra due to the shorter grating period of 25 mm than that of the simulated parameter. The harmonics are beyond the observation limit of VNA. The resonances shown in the transmission spectrum matched exactly with the reflection spectrum and the experimental results matched well with the simulated results in terms of resonant frequency, strength and Q-factor. The experimentally measured resonant frequency also matched well with those calculated by the Bragg condition. The transmission spectrum shows a relatively low transmission loss ($\leq$ 1 dB) indicating that the hole-drilling method did not incur significant loss to the cable. The Q-factor of the resonant peak was 40.8 using the definition of Q-factor in resonant circuit, $Q = f_0/\Delta f$, where f_0 is the resonant frequency and Δf is the 3dB bandwidth in resonant frequency.

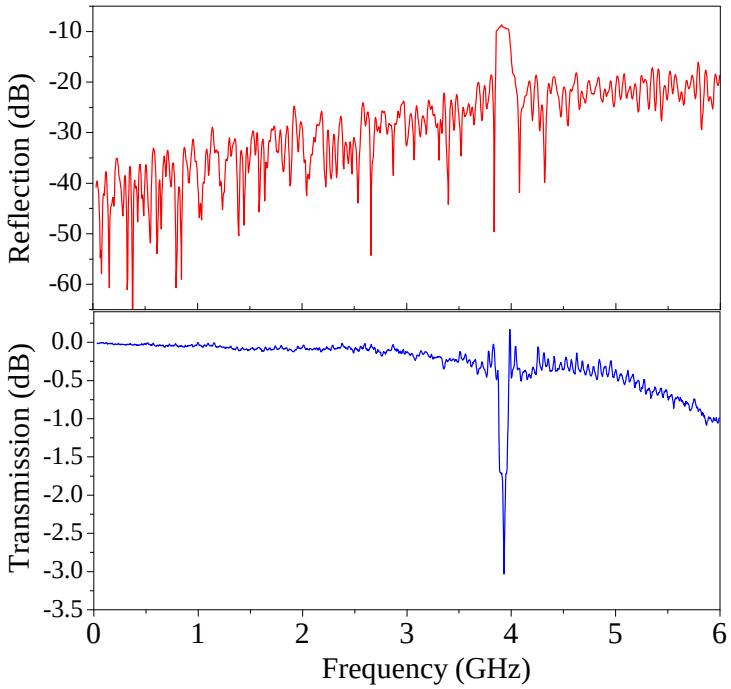

Figure 3.3. Reflection and transmission spectra of the fabricated CCBG.

3.2. CCBG PERFORMANCE ENHANCEMENT

3.2.1. A Positive Feedback System. Similar to a FBG based fiber ring laser [38-40], a positive feedback system was also developed to create oscillation at the resonant frequency of a CCBG device to further enhance the Q-factor, as shown in Fig.3.4. The positive feedback system consists of an electronic-controllable gain-adjustable amplifier worked with the bandwidth-adjustable band-pass filter to provide a narrow band amplification of the radio-frequency (RF) signal covering the fundamental frequency region of the CCBG and get rid of the harmonics. The positive feedback is realized by employing a commercialized directional coupler (DC). The CCBG was terminated by a 50Ω matched load and connected to Port 1 of the DC. Besides a positive feedback, the Barkhausen conditions (i.e. loop gain must be unity and loop phase shift must be 0˚) have to be satisfied in order to start an oscillation. Due to the Bragg grating reflections, the RF signal at Port 1 is extremely low (i.e. $\leqslant$ -40dB) except that at the resonant frequency, as shown in Fig. 3.3. The center frequency and the bandwidth of the adjustable filter can be electronically controlled so as to make narrow-band amplification around the resonant frequency. The condition of unity loop gain can be satisfied at the resonant frequency by adjusting the gain of the amplifier. The loop phase can be tuned to zero at the resonant frequency by changing the length of the coaxial cables. As long as these two conditions are satisfied, signal at resonant frequency starts to oscillate, while the signal at the other frequencies does not oscillate because the Barkhausen conditions are not satisfied. Consequently, a sharp peak was formed at resonant frequency if measured at the isolated end of the DC.

To qualitatively explain the operation principle of the positive feedback system, it can be understood as a “Maser” (microwave laser) system to select and amplify the signal. Just like an Erbium-doped fiber (EDF) ring laser system using a FBG as the bandpass filter. In this case, the CCBG is served as filter, and meanwhile, the amplifier and the Direct Current power supply were served as the gain medium and the pump source, respectively.

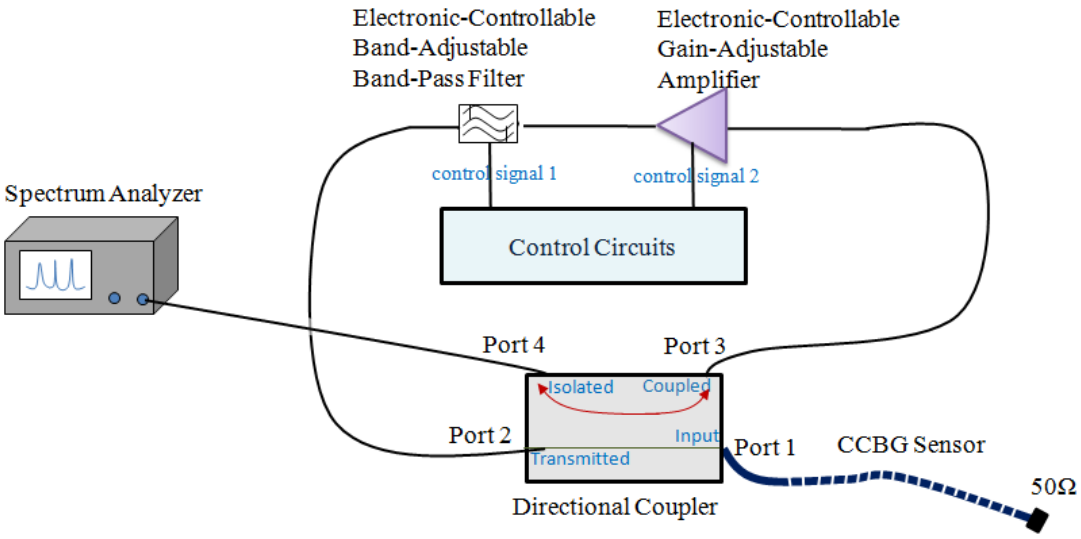

Figure 3.4. A positive feedback system for Q-factor enhancement of a CCBG device.

Verification this "maser" oscillator system was conducted using the CCBG sample fabricated by the hole-drilling method. The center frequency of the electronic bandpass filter was adjusted to be about 3.854 GHz, with a bandwidth of 100 MHz in order to generate oscillation at the fundamental frequency. The reflection loss of the CCBG sensor at the fundamental resonance was -11 dB, the coupling coefficient of the DC was -6 dB from 2 GHz to 8 GHz, the insertion loss of the bandpass filter was about -11 dB, the insertion loss of the DC was about -1dB at the frequency of interest, and cable loss was about -1dB. Since the overall loop loss is counted to be 30 dB, the net gain of the amplifier was tuned to be 30 dB to make the system oscillate at 3.854 GHz. The output signal was observed at Port 4 by a RF spectrum analyzer (Rohde & Schwarz FSU) as shown in Fig. 3.5. The signal to noise ratio of the spectrum was more than 70dB, which is drastically greater than the passive CCBG data in Fig. 3.3. The Q factor of this resonant peak was 17729, which was more than 3500 times greater than of the CCBG itself. The resolution bandwidth (RBW) of the spectrum analyzer was set to be 7 KHz. Sharper resonances could be obtained with smaller RBW value.

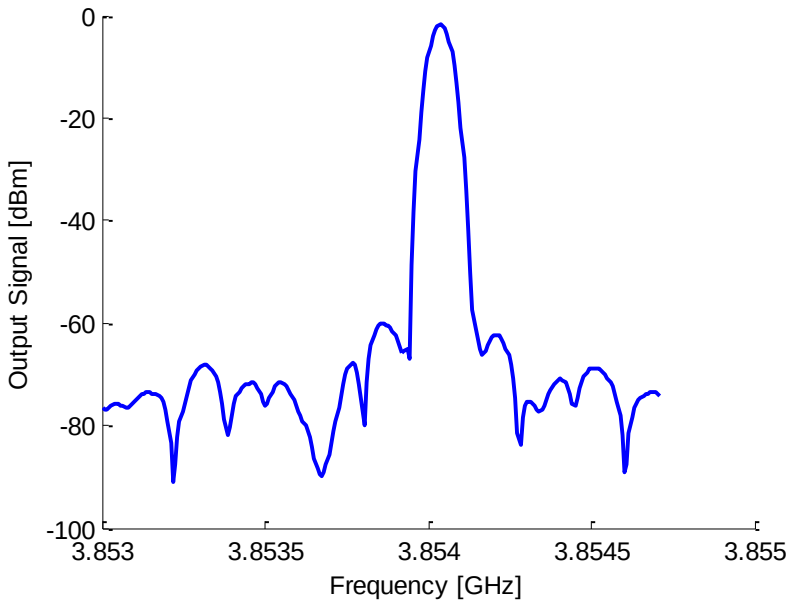

Figure 3.5. Output spectrum of a "maser" system with a bandpass filter induced by a CCBG device.

3.2.2. Coiled Coaxial Cable Resonator. In order to further enhance the Q-factor of the transmission spectrum of the CCBG, we developed a spiral CCBG device called coiled coaxial cable resonator. Figure 3.6 shows the image of a coiled coaxial cable resonator. The coaxial cable (50 Ω, Jamco Electronics, RG-58) was wrapped on a 8.1 mm diameter metallic rod and fixed with a pre-strain as shown in Fig. 3.6. A milling bit (diameter: 1/12 inch) was then used to mill a straight line (red arrow in Fig. 3.6) with the milling depth of 2.1 mm. It is still a Bragg grating structure with multiple periodic discontinuities after straighten the cable . However, the coiled CCBG has a unique performance compared to the straight CCBG.

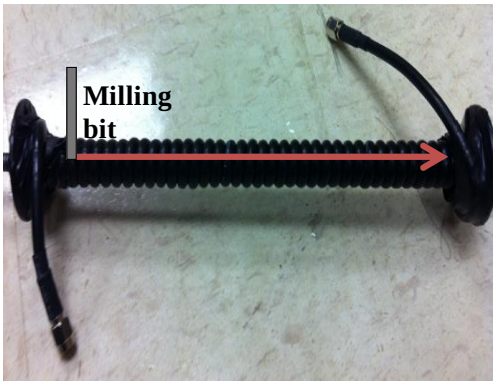

Figure 3.6. Image of a coiled coaxial cable resonator.

In this experiment, no extra lost was observed in the transmission spectrum recorded by a VNA. The transmission spectra (S_{21}) were recorded for each milling point. Figure 3.7 plots the transmission spectra of the coiled coaxial cable resonator as the milling points increased. It is obvious that the strength of the fundamental resonant dip increased and then decreased as the milling points increased. The maxima resonant dip occurred at the 28th discontinuity. The strength of the second harmonic resonances continuously increased as the milling points increased. This can be qualitatively explained by the mutual coupling phenomenon: under coupling, critical coupling and over coupling. The second harmonic resonances were still in under coupling states when the milling points up to 40.

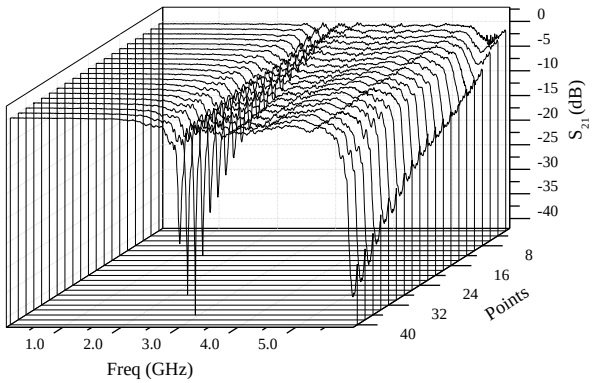

Figure 3.7. Transmission spectra of coiled coaxial cable resonator as the milling points increased.

Figure 3.8 shows the comparison of transmission spectra of straight and coiled CCBGs. The red line represents the coiled CCBG, which has a higher Q-factor of the fundamental resonance (2.462×10^3) than that of the straight CCBG (black line). The strength of the fundamental resonance in the coiled CCBG was over 50 dB, indicating higher measurement accuracy when it is used as a sensor. We are still working on the theoretic modeling part of the coiled device.

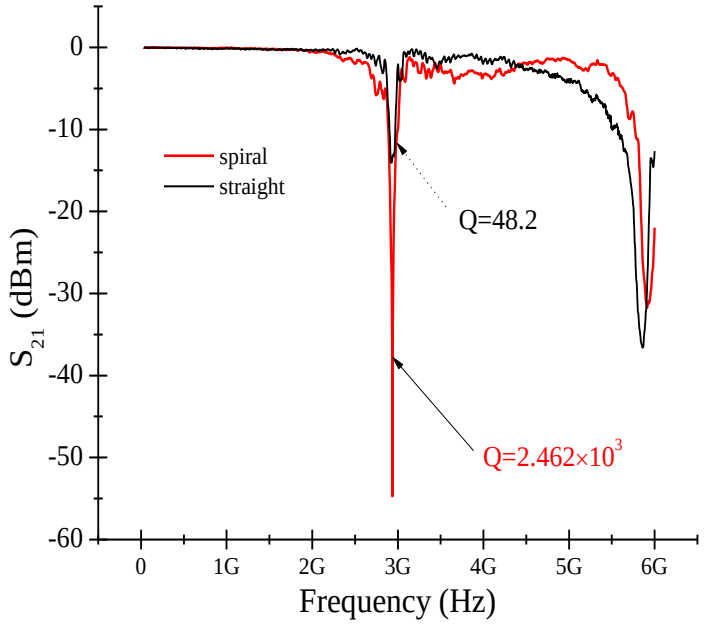

Figure 3.8. Comparison of transmission spectra of straight and coiled CCBGs.

4. EXPERIMENTAL RESULTS

4.1. STRAIN MEASUREMENT OF CCBG

4.1.1. Strain test of the proposed CCBG. A series of CCBGs were used for large strain test. Dynamic range and detection limit of the CCBG sensors have been experimentally investigated.

4.1.1.1 Dynamic range test. For axial tensile strain test, the CCBG of 1 m in length was mounted on a load frame (MTS 880 by TestResources Inc.) using two home machined aluminum clamper and the signals were interrogated by a VNA. The picture of the stain test system was shown in Fig. 4.1. The reflection and transmission spectra of the CCBG with and without the clamping fixtures had no evident difference, indicating that the clampers did not introduce noticeable impedance mismatch and reflections. At each increasing step, the transmission and reflection spectra of the device were recorded to find the resonant frequencies. The VNA was configured to acquire the fundamental resonant peak in the reflection spectrum with an observation bandwidth from 3.5 to 4.5 GHz, a total of 1601 sampling points and intermediate frequency bandwidth (IFBW) of 10 KHz.

To test the dynamic range of the CCBG, the load frame elongated the CCBG at a step of 3 mm, corresponding to a strain increasing step of 3000 με, given the initial distance between the two clampers was 1 m. More than 15 loading steps were applied to the CCBG using the load frame until the cable broke. Several CCBGs with the same fabrication parameters were tested. The average breaking point (inner conductor broke first) was around 5%, indicating the dynamic range of CCBG is dramatically greater than 0.4% which is the maximum tensile strain of a typical FBG. For each strain point the reflection and transmission spectra were measured multiple times consecutively, and the averaged spectra were used to find the center frequency of the resonant peaks or dips. Fourth-order polynomial curve-fitting was used to smooth the resonant peak for further improvement of the measurement accuracy. Figure 4.2 shows the one of the recorded reflection spectra shift as a function of the applied axial strain. The green line represents the point where the CCBG was broken and a high reflection occurred.

Figure 4.1. Image of the strain test system.

Figure 4.3 plots the change in resonant frequency as a function of the applied tensile strain. In general, the resonant frequency of CCBG decreased almost linearly with a slope of -2.1 KHz/με, which matched well with the calculated slope using equation (11). The linear strain-frequency relation indicates that the CCBG can be used as a sensor for strain measurement after it is properly calibrated. The dynamic range of 5% indicates the proposed CCBG may provide a solution to the problem of limited dynamic range faced by FBG in SHM. An interesting observation during the experiments was that the Q-factor decreased as the load strain increased. This can be qualitatively explained that the changes in dimension of the cable as the increased strain will induce an impedance mismatch to increase the signal loss of the cable, but the decreasing of Q-factor did not influence the linearity and sensitivity of CCBG. The strain-frequency relation of a CCBG at a reduced step size of 300 με was also shown in the inset of Fig. 4.3. The strain-frequency response was also linear enough.

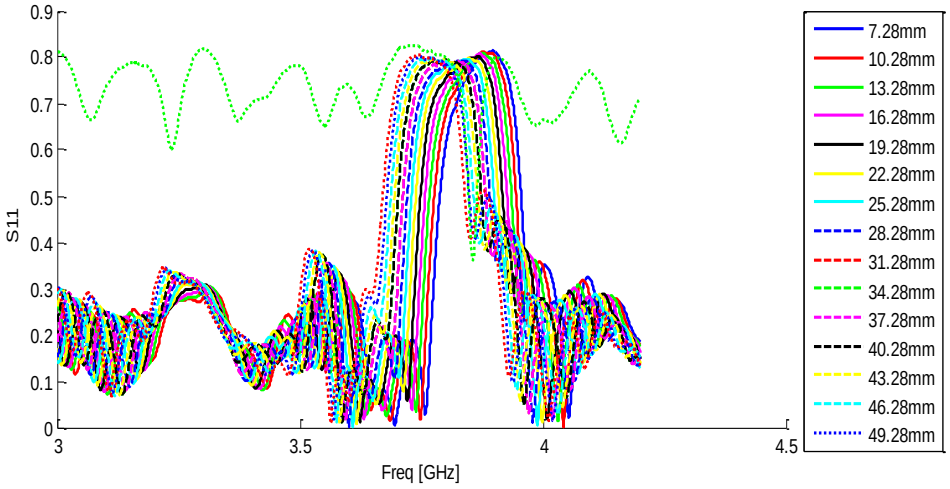

Figure 4.2. Reflection spectra shift as strain increased.

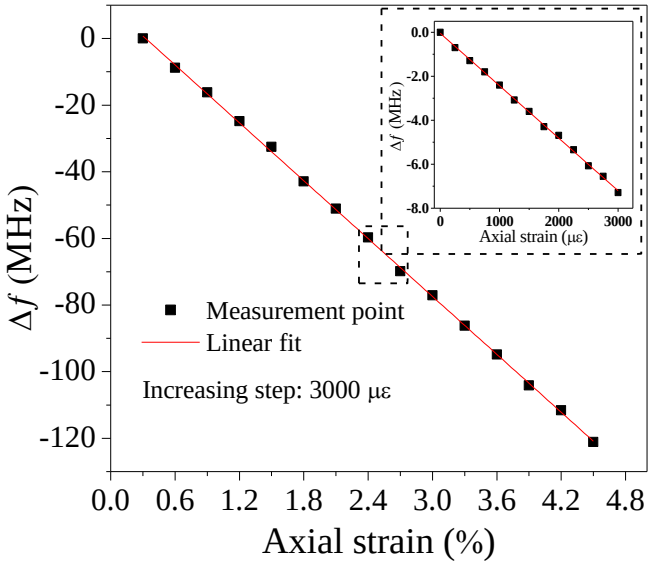

Figure 4.3. Resonant frequency as a function of strain: dynamic range test of CCBGs.

4.1.1.2 Detection limit test. For the detection limit test of the proposed CCBG, the load frame elongated the CCBG at a step of 0.1 mm, corresponding to a strain increasing step of 100 με. A prestressing load was applied to eliminate the measurement error and 20 loading steps were applied to the CCBG. The observation bandwidth of VNA was set to 100 MHz around resonant frequency to further enhance the measurement

accuracy. In practical measurements especially at small increasing steps, noise from random reflections along the cable as well as the thermal noise present in the interrogation instruments are unavoidable. To detect the small resonant-frequency shift and achieve high resolution in large strain measurement, a cross-correlation post-processing method was used. The cross-correlation between the two spectra (before and after applying strain) results in a peak whose location provides a direct measure of the resonant-frequency shift. Using the cross-correlation method, every point in the spectra will contribute to further enhance the measurement accuracy. Figure 4.4 plots the change in resonant frequency as a function of axial strain. With this post-processing method, the strain-frequency response was linear enough, indicating a high resolution of 100 με for the proposed CCBG.

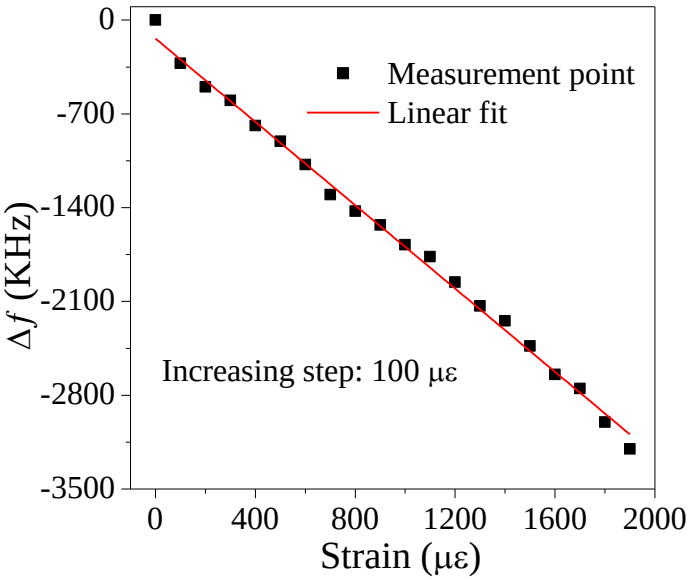

Figure 4.4. Resonant frequency as a function of strain: detection limit test of CCBGs.

4.1.2. Strain Test of CCBG with the Positive Feedback System. To further improve the detection limit, the proposed positive feedback system in Section 3.2.1 was applied. Using the same strain test system to monitor the spectra through a RF spectrum analyzer other than a VNA, the elongated steps were set at 100 με and 20 με, respectively.

Figure 4.5 shows the spectra shift with different increasing steps. Figure 4.5 (a) and (b) plot the "maser" spectra shift with loading step of 100 με and 20 με, respectively. It is obvious that the measurement accuracy was further enhanced due to the higher signal-to-noise ratio (SNR, >55dB) and smaller 3dB linewith of the reflection spectra. The strain-frequency response could be achieved just by simply tracking the frequencies of resonances. Figure 4.6 shows the frequency-strain relationship. Figure 4.6 (a) and (b) plot the "maser" frequency shift as a function of applied strain. A tensile strain of 20 με could be clearly resolved with a linear slope of – 1.69 kHz/με. A standard deviation of ± 16 kHz can be resolved through two hours stability test indicating a higher resolution of ± 10 με. The CCBG performance can be enhanced via the proposed positive feedback system.

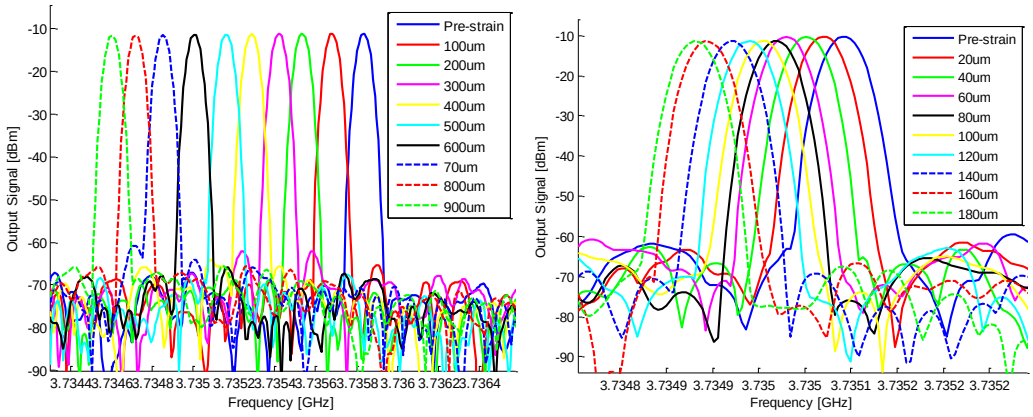

(a) (b)

Figure 4.5. Spectra shift with different increasing steps. (a) 100 με (b) 20 με.

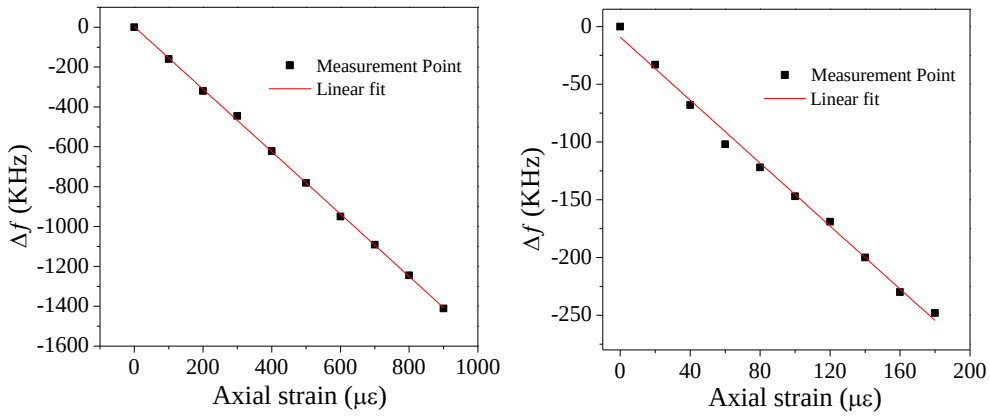

(a) (b)

Figure 4.6. Resonant frequency shift as a function of axial strain with different increasing steps. (a) 100 με (b) 20 με.

4.2. TEMPERATURE RESPONSE OF CCBG

In the temperature test, two types of coaxial cables (RG-58 flexible coaxial cable 50Ω and semi-rigid coaxial cable 50Ω) were used for fabricating CCBGs. A VNA was used to in situ monitor the reflection spectrum (S_{11}) of the CCBG. One end of the CCBG was connected to Port 1 of the VNA using an extension cable and the other end was connected to a 50Ω terminator. The CCBG sensing part was placed into a tubular furnace (Lindberg/Blue M). The temperature of the furnace was set to increase at a step of 10 ℃ and the dwelling time was set to be 30 minutes at each step. The VNA was calibrated before testing with a sampling point of 1601, IFBW of 1 KHz and sampling bandwidth of 500MHz (3.7GHz to 4.2GHz). In order to further enhance the testing data accuracy, 16 times average was applied at each testing point.

Figure 4.7 plots the resonant frequency shifts of the RG-58 flexible CCBG and semi-rigid CCBG as a function of ambient temperature. The black and red dots represent the temperature response of the flexible CCBG and the semi-rigid CCBG, respectively. The flexible CCBG are more sensitive to the ambient temperature with a slope around 0.327 MHz/ ℃, which has a potential of being a temperature sensor. It also could be applied to investigate the coefficient of thermo-expansion (CTE) of different dielectric materials. The semi-rigid CCBG is a good candidate for strain measurement because of

its temperature insensitivity and robustness to survive harsh condition, which may enable new applications in SHM. In addition, the flexible CCBG and semi-rigid CCBG can be used for simultaneous measurement of temperature and strain.

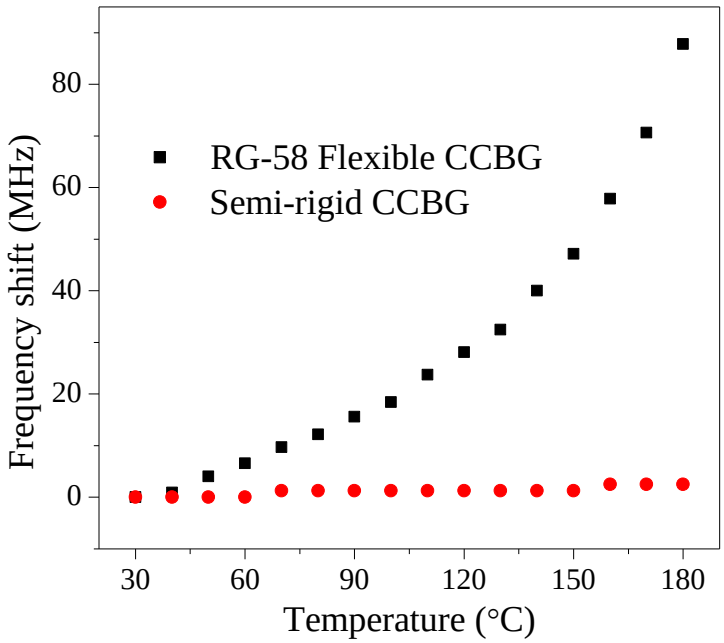

Figure 4.7. Resonant frequency shift of the RG-58 flexible CCBG and semi-rigid CCBG as a function of ambient temperature.

5. CONCLUSIONS AND FUTURE WORK

5.1. CONCLUSIONS

To summarize, this thesis proposes a novel CCBG device as a sensor for structural health monitoring applications. The device was fabricated by drilling holes into the coaxial cable at periodic distances along the cable axis. The open hole resulted in an impedance or refractive index discontinuity and partial reflection of the EM wave propagating inside the cable. The periodic discontinuities produced resonant peaks and dips in reflection and transmission spectra, respectively. These resonances occurred at discrete spectral positions with a fundamental frequency and high order harmonics. No noticeable loss to the EM waves was observed at frequencies other than the resonances. A positive feedback system and a coiled coaxial cable resonator were developed to further enhance the CCBG performance. To better understand the physics, the S-parameters of the open hole was calculated using finite element analysis and the device was modeled based on a T-matrix method. The theoretic simulation and experimental result matched well. The experimentally measured resonant frequencies also matched well with those calculated by the Bragg equation. The sensing mechanism has been fully investigated and matched well with the experimental results. When subject to a strain, the resonant frequency of the CCBG device showed a linear response to the loaded strain, indicating the CCBG's potential capability of being used as a strain sensor with a large dynamic range of about 5%. The resolution of CCBG as a strain sensor was 100 με. A positive feedback oscillation system and a coiled coaxial cable resonator were also developed to enhance the Q-factor for further improvement of measurement accuracy. The experimental results showed that the CCBG sensors performed well for large strain measurement needed in structural health monitoring (SHM).

The temperature responses of CCBGs made of different types of coaxial cables were also investigated. CCBG can be used as a temperature sensor by tracking the shift in resonant frequency as a function of temperature. And CCBGs made of different cables have dramatically different temperature sensitivity (e.g., order of magnitude difference observed for the flexible cable (RG-58) and the semi-rigid cable). Cables with different

temperature sensitivities can be used for simultaneous measurement of strain and temperature.

5.2. FUTURE WORK

[1] Investigate the theoretic modeling of the coiled coaxial cable resonator.

[2] Develop distributed ceramic or sapphire waveguide Bragg gratin in radio (or microwave) frequency for applications in high temperature harsh environment.

[3] Develop embedded sensors into components and structures for distributed health monitoring (e.g., crack, deflection, vibration and corrosion) in extreme environments.

BIBLIOGRAPHY

[1] K. Sukun, S. Pakzad, D. Culler, J. Demmel, G. Fenves, S. Glaser, and M. Turon, "Health Monitoring of Civil Infrastructures Using Wireless Sensor Networks," in *Information Processing in Sensor Networks, 2007. IPSN 2007. 6th International Symposium on*, 2007), 254-263.

[2] J. Leng and A. Asundi, "Structural health monitoring of smart composite materials by using EFPI and FBG sensors," Sensors and Actuators A: Physical **103**, 330-340 (2003).

[3] T. Nobuo, "Characterization of microscopic damage in composite laminates and real-time monitoring by embedded optical fiber sensors," International Journal of Fatigue **24**, 281-289.

[4] A. D. Kersey, T. A. Berkoff, and W. W. Morey, "Multiplexed fiber Bragg grating strain-sensor system with a fiber Fabry?Perot wavelength filter," Opt. Lett. **18**, 1370-1372 (1993).

[5] A. D. Kersey, M. A. Davis, H. J. Patrick, M. LeBlanc, K. P. Koo, C. G. Askins, M. A. Putnam, and E. J. Friebele, "Fiber grating sensors," Lightwave Technology, Journal of **15**, 1442-1463 (1997).

[6] A. Mehta, W. Mohammed, and E. G. Johnson, "Multimode interference-based fiber-optic displacement sensor," Photonics Technology Letters, IEEE **15**, 1129-1131 (2003).

[7] Y.-J. Rao, Y.-P. Wang, Z.-L. Ran, and T. Zhu, "Novel Fiber-Optic Sensors Based on Long-Period Fiber Gratings Written by High-Frequency CO 2 Laser Pulses," J. Lightwave Technol. **21**, 1320 (2003).

[8] H.-N. Li, D.-S. Li, and G.-B. Song, "Recent applications of fiber optic sensors to health monitoring in civil engineering," Engineering Structures **26**, 1647-1657 (2004).

[9] C. Hautamaki, S. Zurn, S. C. Mantell, and D. L. Polla, "Experimental evaluation of MEMS strain sensors embedded in composites," Microelectromechanical Systems, Journal of **8**, 272-279 (1999).

[10] N. Chaimanonart and D. J. Young, "Remote RF powering system for wireless MEMS strain sensors," Sensors Journal, IEEE **6**, 484-489 (2006).

[11] E. Schedin and A. Melander, "The evaluation of large strains from industrial sheet metal stampings with a square grid," Journal of Applied Metalworking **4**, 143-156 (1986).

[12] I. Aoki and T. Takahashi, "Material flow analysis on shearing process by applying Fourier phase correlation method—analysis of piercing and fine-blanking," Journal of Materials Processing Technology **134**, 45-52 (2003).

[13] J. Dupre, M. Cottron, and A. Lagarde, "Grating interrogations: from small to large strain measurement," Experimental Mechanics **35**, 153-158 (1995).

[14] R. Rotinat, R. bi Ti é, V. Valle, and J. C. Dupr é, "Three Optical Procedures for Local Large-Strain Measurement," Strain **37**, 89-98 (2001).

[15] V. Bhatia, K. A. Murphy, R. O. Claus, T. A. Tran, and J. A. Greene, "Recent developments in optical-fiber-based extrinsic Fabry-Perot interferometric strain sensing technology," Smart Materials and Structures **4**, 246 (1995).

[16] M. Silva-L ópez, A. Fender, W. N. MacPherson, J. S. Barton, J. D. C. Jones, D. Zhao, H. Dobb, D. J. Webb, L. Zhang, and I. Bennion, "Strain and temperature sensitivity of a single-mode polymer optical fiber," Opt. Lett. **30**, 3129-3131 (2005).

[17] Z. Xiong, G. D. Peng, B. Wu, and P. L. Chu, "Highly tunable Bragg gratings in single-mode polymer optical fibers," Photonics Technology Letters, IEEE **11**, 352-354 (1999).

[18] S. Liehr, P. Lenke, M. Wendt, K. Krebber, M. Seeger, E. Thiele, H. Metschies, B. Gebreselassie, and J. C. Munich, "Polymer Optical Fiber Sensors for Distributed Strain Measurement and Application in Structural Health Monitoring," Sensors Journal, IEEE **9**, 1330-1338 (2009).

[19] K. Sharon, P. Kara, H. Tasnim, and K. Mervyn, "Behaviour of intrinsic polymer optical fibre sensor for large-strain applications," Measurement Science and Technology **18**, 3144 (2007).

[20] P. J. Nahin, *Oliver Heaviside, sage in solitude : the life, work, and times of an electrical genius of the Victorian age* (IEEE Press, New York, 1987).

[21] R. E. Matick, "Transmission line pulse transformers—Theory and applications," Proceedings of the IEEE **56**, 47-62 (1968).

[22] G. Keiser, "Optical Fiber Communications," in *Wiley Encyclopedia of Telecommunications* (John Wiley & Sons, Inc., 2003).

[23] M. M. Sanchez-Lopez, A. Sanchez-Merono, J. Arias, J. A. Davis, and I. Moreno, "Observation of superluminal and negative group velocities in a Mach--Zehnder interferometer," Applied Physics Letters **93**, 074102-074103 (2008).

[24] M. d. M. Sanchez-Lopez, J. A. Davis, and K. Crabtree, "Coaxial cable analogs of multilayer dielectric optical coatings," American Journal of Physics **71**, 1314-1319 (2003).

[25] G. J. Schneider, S. Hanna, J. L. Davis, and G. H. Watson, "Defect modes in coaxial photonic crystals," Journal of Applied Physics **90**, 2642-2649 (2001).

[26] A. Hach é and L. Poirier, "Anomalous dispersion and superluminal group velocity in a coaxial photonic crystal: Theory and experiment," Physical Review E **65**, 036608 (2002).

[27] G. D. Chen and D. Pommerenke, "Novel Distributed Cable Sensors for Detection of Cracks in RC Structures," AIP Conference Proceedings **820**, 1343-1350 (2006).

[28] G. Chen, H. Mu, D. Pommerenke, and J. L. Drewniak, "Continuous coaxial cable sensors for monitoring of RC structures with electrical time domain reflectometry," in (SPIE, 2003), 410-421.

[29] B. S. Kawasaki, K. O. Hill, D. C. Johnson, and Y. Fujii, "Narrow-band Bragg reflectors in optical fibers," Opt. Lett. **3**, 66-68 (1978).

[30] A. Ezbiri, S. E. Kanellopoulos, and V. A. Handerek, "High resolution instrumentation system for fibre-Bragg grating aerospace sensors," Optics Communications **150**, 43-48 (1998).

[31] J. Frieden, J. Cugnoni, J. Botsis, T. Gmür, and D. Ćorić, "High-speed internal strain measurements in composite structures under dynamic load using embedded FBG sensors," Composite Structures **92**, 1905-1912 (2010).

[32] S. Oh, W. Han, U. Paek, and Y. Chung, "Discrimination of temperature and strain with a single FBG based on the birefringence effect," Opt. Express **12**, 724-729 (2004).

[33] R.-S. Shen, J. Zhang, Y. Wang, R. Teng, B.-Y. Wang, Y.-S. Zhang, W.-P. Yan, J. Zheng, and G.-T. Du, "Study on high-temperature and high-pressure measurement by using metal-coated FBG," Microwave and Optical Technology Letters **50**, 1138-1140 (2008).

[34] L. Ren, H.-N. Li, L. Sun, and D.-S. Li, "Development of tube-packaged FBG strain sensor and application in the vibration experiment of submarine pipeline model," in (SPIE, 2005), 98-103.

[35] T. Erdogan, "Fiber grating spectra," Lightwave Technology, Journal of **15**, 1277-1294 (1997).

[36] D. B. Davidson, "Computational Electromagnetics for RF and Microwave Engineering - [Book Review]," Aerospace and Electronic Systems Magazine, IEEE **20**, 27-28 (2005).

[37] E. Li, "Temperature compensation of multimode-interference-based fiber devices," Opt. Lett. **32**, 2064-2066 (2007).

VITA

Jie Huang was born in Shandong, China. In June 2009, he obtained a bachelor's degree in Department of Opto-electronics Information Engineering, College of Precision Instrument and Opto-electronics Engineering from Tianjin University, Tianjin, R.P. China.

In August 2010, he enrolled at Missouri University of Science and Technology to pursue a master's degree of Electrical and Computer Engineering under the guidance of Dr. Hai Xiao. His research interest is RF based devices and fiber optic sensors.